Model-assisted ultrasonic calibration using intentionally embedded defects for in-process weld inspection
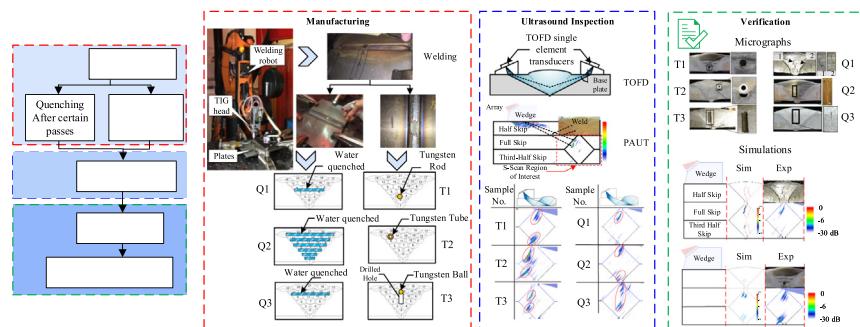
Ehsan Mohseni *, Yashar Javadi, Nina E. Sweeney, David Lines, Charles N. MacLeod, Randika K.W. Vithanage, Zhen Qiu, Momchil Vasilev, Carmelo Mineo, Peter Lukacs, Euan Foster, S. Gareth Pierce, Anthony Gachagan

Centre for Ultrasonic Engineering (CUE), Department of Electronic and Electrical Engineering, University of Strathclyde, Glasgow G1 1XQ, UK

HIGHLIGHTS

- Tungsten tubes could be successfully used for reference amplitude and gain calibration purposes.
- CIVA as a simulation tool was found to provide reliable predictions for the weld inspections.
- Local inter-pass water quenching of the weld can introduce cracks in the weld.
- Water quenching-induced cracks and tungsten inclusions can be successfully detected by phased array ultrasound.

GRAPHICAL ABSTRACT

ARTICLE INFO

ABSTRACT

Automated in-process Non-Destructive Testing (NDT) systems are rapidly gaining traction within the manufacturing industry as they reduce manufacturing time and costs. When considering calibration and verification of such systems, creating defects of known geometry and nature during the deposition of a weld can: (I) help examine the capability of the automated system to detect and characterise defects, (II) be used to form a database of signals associated with different defect types to train intelligent defect classification algorithms, and (III) act as a basis for in-process gain calibration during weld inspection at high temperatures, where the ultrasound beam can be skewed as a result of velocity gradients. In view of this, this paper investigates two unique methodologies for introducing: (a) lack of fusion weld defects by embedding tungsten in the weld and (b) creating artificial weld cracks by quenching to imitate the real cracking scenarios. According to the results of Phased Array Ultrasound Testing (PAUT) inspections, the methodologies used for embedding the artificial defects were successful. The validity of inspections was also verified by extracting micrographs from the defective sections of the welds, and model-based simulations were carried out to gain a better understanding of the wave propagation path and interaction with the generated defects.

1. Introduction

Welding, as one of the main manufacturing processes utilised across different industries to join two pieces of metal together, is often accompanied by undesirable internal defects that can adversely affect the integrity of the finished components, and thus reduce their expected life span [1,2]. A broad range of defect types may occur in the weld where the formation of some types is promoted under certain circumstances. As an example, Lack of Fusion (LoF) defects and cracking are two bulk defects that can be found frequently in welded joints, where the first one is created during manufacturing [3] and the latter can be a delayed defect triggered by hydrogen, microstructure and residual stresses [4]. Welded components are inspected using Non-Destructive

* Corresponding author.
E-mail address: Ehsan.mohseni@strath.ac.uk (E. Mohseni).

Testing (NDT) methods, after the manufacturing process, to detect possible weld discontinuities and to make a further decision (*i.e.* acceptance/rejection) regarding the parts [5].

1.1. Non-destructive testing

Ultrasonic Testing (UT) has been actively used for the inspection of welds for decades [6,7] and regulated by well-established standards such as BS EN ISO 17640 and BS EN ISO 19285. In the concept of these standards, the signal amplitude of a calibration feature is taken as the reference and according to the ratio of the signal amplitude of a reflector to the amplitude of the reference, the reflectors are categorized as defects/non-defects. However, the NDT community has started to accept the fact that the severity of a defect cannot be judged solely based on its signal amplitude [8]. As an example, a very long stress crack with a very tight opening (kissing bonds), can have a very smaller UT signal amplitude as compared to the less critical LoF defect, particularly when the loading conditions are acting to minimize crack opening.

Therefore, it is crucial to investigate the nature of indications from common weld defects by introducing them deliberately into the weld and gain a better understanding of their signal amplitude levels. This information could serve as an optimiser of in-process gain calibration [9]. The importance of being able to produce weld-defects that simulate realistic defects can be explained through several reasons and finds meaning in the context of in-process automated inspection. As previously mentioned, such defects are beneficial to achieve a better definition of calibration gains, and they can also be used for training purposes [10].

Moreover, an inspection of the weld region at high temperatures while welding is in progress challenges the classic calibration strategy and emphasizes the importance of having in-process intentional defects for the purpose of calibration. It should be noted that there will always be the final inspection as per the code standards when the sample reaches room temperature. The in-process inspection aims to detect and correct defects during manufacturing so that there will be no buried defects at the final inspection stage. A key benefit of having known reflectors in the weld is to assist in calibrating the compensations for the elevated temperatures and thermal gradients. During the in-process inspection strategy, the acoustic path of an ultrasonic shear beam formed to inspect the weld geometry at elevated temperatures is significantly different from the path that the same beam would follow in a welded plate at room temperature [11,12]. The acoustic properties, particularly the sound velocity, of the weld region and Heat-Affected Zone (HAZ) changes as the sound traverses these zones, causing the beam to bend within the material, skewing its trajectory such that it does not reach the point it is intended to – see Fig. 1. This deviation of the beam path at high temperatures delivers indications with lower amplitudes at an erroneous position for a certain feature in the weld [13,14]. Therefore, an instrument gain, set according to UT inspections of a calibration

welded piece at room temperature, cannot be the basis for conducting inspections at high temperatures. In such a case, one scenario is to have a duplicate of the component, with embedded reference reflectors undergoing the same thermal process as the main component at the same time. Intentional calibration defects of a known size can be introduced into the duplicate sample at known locations as the weld is being carried out. This approach can account for the weld temperature gradient while the gain is being calibrated however, it is a costly approach to undertake.

Furthermore, gaining a better understanding of defect signals is essential for an autonomous Non-Destructive Evaluation (NDE) system comprised of an automated inspection unit, which is very commonly done by robotic systems, and an intelligent algorithm for signal interpretation [15,16]. The latter mainly refers to artificial intelligence systems that use machine learning techniques to recognize, categorize, and size defects based on the results of the automated inspection [17–19]. The performance of such systems strongly relies on the relevance and completeness of the training data provided to the system [20,21]. For instance, a system trained only with the signals of LoF defects is not able to discriminate a crack indication from the one for an LoF defect. Thus, the first step toward forming such an intelligent system is to comprehend the amplitude relationship between these defects and the signal pattern associated with each defect type.

Phased Array Ultrasonic Technology (PAUT) has been the preferred method of inspecting the thick weld sections in joints, tubes, and pressure vessels since the time of its emergence [22]. The superiority of PAUT over other conventionally used NDT methods is readily recognized in many industrial sectors such as chemical, petrochemical, transportation, and nuclear. When compared with radiography, another long-standing weld inspection method, PAUT has the advantage of providing signal response data, which is critical for the new NDT acceptance criteria concepts such as fitness-for-purpose life estimation approaches [22–24]. As a second advantage, when compared to radiography, the UT operator is not subjected to hazardous radiation during the test operation [25,26]. Furthermore, PAUT provides a better detectability for cracks and defects with tight openings where the competency of radiography falls short [26]. Other NDT methods that have recently been adopted for weld inspection, such as surface eddy current arrays, are still incapable of providing adequate penetration depth when used on ferromagnetic weld sections thicker than a few millimeters [27]. PAUT is very flexible, on account of the time delays that can be applied to the excitation of multiple elements, ordered in rows and columns, to steer and/or focus the beam. It is also possible to use a subset of elements, so-called sub-apertures, to sweep a beam across the entire aperture of the array [28]. Beam steering using linear arrays enables the user to keep the array at a stationary position while sweeping the beam to reach inaccessible regions of a part through an angle range. This makes the beam steering suitable for weld inspection where probes cannot usually be placed on the weld crown directly; and hence, the inspections are done from the sides [26].

The results of the sweep are normally plotted as a Sectorial Scan (S-scan) image, where the A-scans associated with different sweep angles are stacked beside each other. It should be noted that the beam angle variation in an S-scan allows the user to get a better signal response from defects of different orientations within the weld. However, implementing such a technique is not without challenges. For example, each beam in the angle sweep can be focused at one point to generate a focused S-scan image. Consequently, the S-scan can provide partially better inspection results for those points at which the beam is focused, whereas the indications from other parts of the weld are captured with lower quality. The problem is normally addressed by the use of dynamic focusing or the newer alternative Full Matrix Capture (FMC), for which full matrix data for all the transmit-receive combinations of the array elements is recorded and the data is post-processed to form an image of the inspected area [29]. One of the post-processing approaches, known as Total Focusing Method (TFM), produces a fully
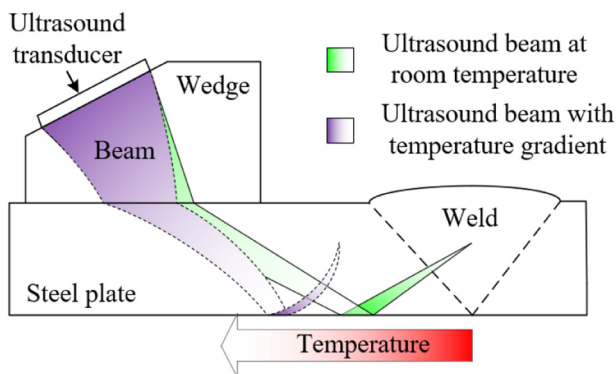

Fig. 1. Effect of temperature gradient in the welded section causing the ultrasound beam to bend and deflect from its original path.

focused image of the weld section which is expected to be superior to the S-scan image as long as the inspected area falls within the nearfield of the array. The FMC data streaming and the TFM image processing are deemed to be time-consuming for real-time visualization of the inspection results, however, the speed can be enhanced significantly (*i.e.* very close to the speed of the S-scan) by gating the time data to capture only for the weld section and truncating the TFM window size to fit the dimensions of the welded area.

The fast-growing computational power provided by advanced electronics makes it possible to have a supporting numerical model and to simulate the experimental observations for a better insight into the problem. Owing to these advances, the phased-array technique and all its different inspection methodologies can be simulated using numerical tools for various test scenarios to verify the inspection results. As one of the tools that is frequently used for ultrasound wave propagation modelling, CIVA is proven to be an efficient software for investigating (I) different inspection scenarios, (II) various sensor designs through parametric studies, and (III) the validity of experimental test results. The semi-analytical solver within CIVA, as compared to the time-consuming finite element solvers, allows to perform quicker modelling and to study the behavior of ultrasound beams as they interact with discontinuities in material [30,31].

1.2. In-process weld inspection and verification

Accordingly, this research, as part of a larger project concerning in-process automated multi-pass weld inspection [14,32], aims to implement novel approaches to generate deliberate weld defects, such as cracks and LoF, within a multi-pass welding process. Therefore, robotically enabled automated multi-pass welding was carried out to manufacture a series of butt-welded steel plates. For each of these welded samples, a different methodology was examined to deliberately create realistic weld defects. After manufacturing the samples with intentional weld-defects, UT inspections were carried out on the samples at room temperature. PAUT S-scans and Time of Flight Diffraction (TOFD) results were analyzed to study the indications amplitude levels and signatures obtained for different intentional defects. Some of the welded samples were sectioned to prepare macrographs from the positions where the intentional defects are embedded. The macrographs were used to verify whether the defect generation methodology had been successful. Semi-analytical models were also prepared in CIVA, according to the macrographic sections, to gain a better insight into the experimental results obtained by PAUT and to clarify any ambiguity concerning inspection indications. Accordingly, the simulation results were compared to the inspection results. The actions undertaken are depicted in Fig. 2, where the research is categorized into three main sections of (I) manufacturing, (II) inspection, and (III) verification.

Section 2 of this manuscript covers the welding procedure, and ultrasound calibrations and inspections. The methods used for introducing intentional defect of known size through embedding tungsten inside the weld, the inspection results for these welded samples, and the modelling results verifying the validity of such defects are presented in Section 3. Then, Section 4 is dedicated to the creation of cracks as intentional weld defects, the inspection results, and the simulations supporting the observations. The conclusions of the study are provided in Section 0 of the manuscript.

2. In-process inspection experimental configuration

2.1. Automated welding configuration

The autonomous welding was performed using an integrated system comprised of a number of components. A 6-axis KUKA robot, as the welder robot, carried a tungsten inert gas (TIG) torch which was connected to a welder, a wire feeder, a high dynamic range camera, and a laser profiler as depicted in Fig. 3(a). The sensors' communication
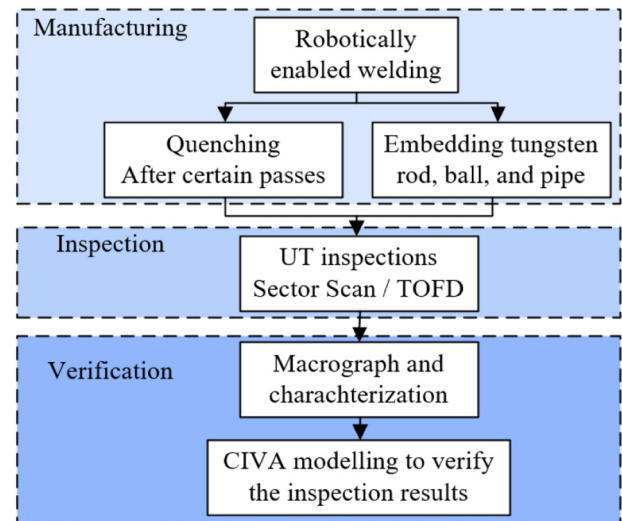

Fig. 2. Flowchart showing the procedure that was followed in the presented research.

with the robot was made possible by a Compact RIO 9038 (cRIO) from National Instruments (NI) and a NI LabVIEW code. The integration of the sensors and the welder robot was achieved through ITRA toolbox which enabled the welder robot to correct its path and to follow the weld groove, as it was welding, by receiving the laser measurements in real-time [33,34]. Plates of structural steel grade (S275) with dimensions of 300 mm × 200 mm × 15 mm and chemical composition as presented in Table 1, were used as the parent material for the weld. Each plate was beveled along one side by 45 degrees, and two of these plates were placed beside each other along their beveled corners to form a 90 degrees V-groove (see Fig. 3(b)). Six clamps were used to tightly fix the plates onto the table. The deposition was carried out using the automated integrated welding system in 21 passes.

A mixture of SUPRAMIG welding wire and hard-facing steel wire was used to fill the groove in different samples. The artificial cracks tended to nucleate and to form easier in the weld when the hard-facing wire with a very high hardness of 54–60 HRC was used. A polished cross-sectional weld macrograph, which was partially filled with the hard-facing wire, is demonstrated in Fig. 3(c). The chemical composition of the wires, used as fillers in the welding process, are listed in Table 1. These material properties were reported according to the datasheets provided by the plate and wire manufacturer. A total number of 6 samples were welded using this system. These samples will be discussed in more detail in Sections 3 and 4.

2.2. Ultrasound inspection

A 5 MHz 64 element linear array of pitch 0.5 mm from Olympus along with a LTPA PAUT controller (by PEAK NDT, UK) was used to perform shear sectorial scans of the welds. A 37.6° wedge was attached to the array and the focal laws were generated to form an S-scan in steel covering a range of angles from 40° to 75°. The wedge was 78 mm in length, 47 mm in height and 40 mm in width. All the inspections were carried out when the samples reach room temperature. An in-house LabVIEW-based software was developed to visualize the S-scan images with superimposed weld overlays.

2.3. Ultrasound inspection calibration

A series of calibrations were carried out prior to the inspection of the welded samples. The procedures provided by BS EN ISO 1764 were closely followed during all the inspections. A preliminary gain calibration step was necessary to perform a quick scan on welds in order to
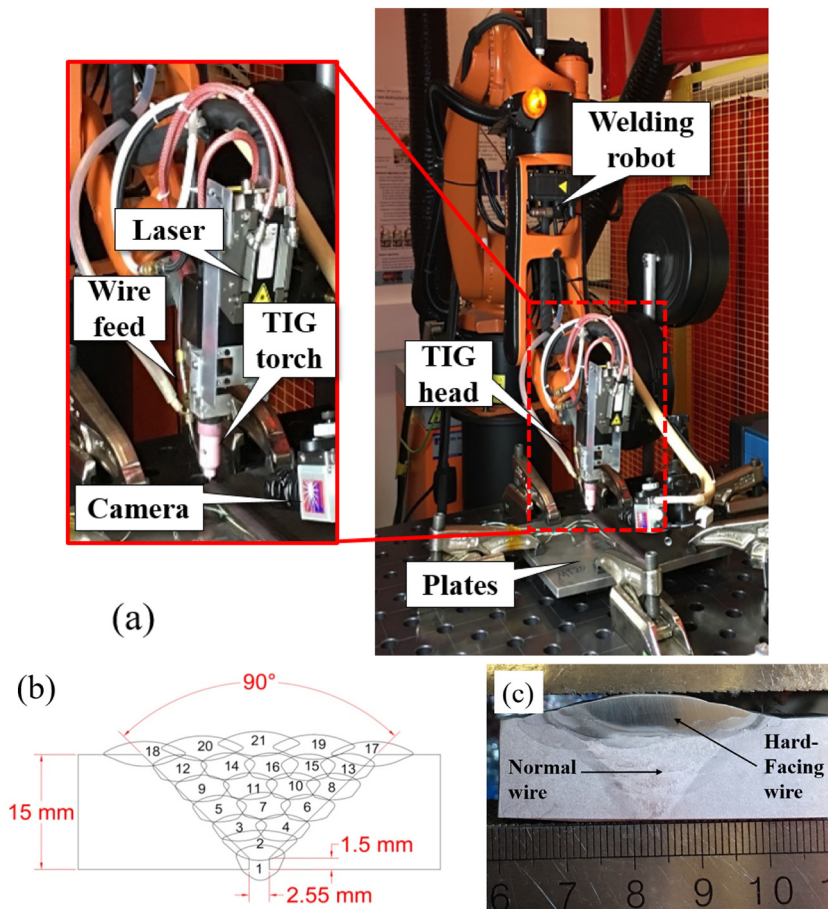
Fig. 3. (a) Integrated system of the autonomous TIG welding unit, (b) A schematic of the weld procedure showing the groove, layers, and passes, and (c) A weld section filled with normal wire and hard-facing wire.

find an almost defect-free section of the weld. Then, such a section could be cut out of the weld and be used to fabricate a calibration sample with Side Drilled Holes (SDHs). To this end, an SDH of Ø 1.5 mm was initially drilled in the middle of the thickness of a 15 mm thick steel plate as shown in Fig. 4(a), and the hole was used to calibrate the gain in the sectorial scans. A transmit voltage of 80 V with a pulse width of 100 ns and a repetition frequency of 20 kHz, and a fixed gain of 30 dB were used in the tests. Subsequently, the signal of the SDH received at an angle of 55° was set to 80% of the screen height. The 55° beam was the central refracted shear beam inside the steel for the selected assembly of the array and the wedge.

Once the preliminary gain calibration was done, all the 6 weld samples were scanned and a defect-free section in one of the samples was marked to be cut. This section was drilled in two places to build the main reference block. Two SDHs of Ø 2 mm were drilled in the weld of this section at the positions depicted in Fig. 4(b). It was essential to carry out the gain calibration on this reference piece from the same spot that the inspections were to be performed on all other samples

since the acoustic properties of the heat-affected zone (HAZ) and weld were dissimilar to those of the parent plate. This was particularly important in the case of the samples built in this study, where the composition of the wires used for welding was different from the composition of the substrate. Therefore, the horizontal position of the wedge relative to the weld centerline was verified using CIVA simulations and it was set as close as possible to the weld without the wedge going on the weld toes, as shown in Fig. 4(c). The simulation also demonstrated that there was at least one angle at which the formed beam was normal incident to the closest weld flank. This was required to check the conformity of inspections with PAUT standards. Inspections were repeated from the opposite side of the weld to get the specular reflection from the opposite weld flank.

After positioning the wedge on the calibration sample, the gain was set to 50 dB in order to set the signal amplitudes of the two SDH indications to 100% of the scale bar as shown in Fig. 5(a). Evidently, the signal amplitudes of these two calibration SDHs were not identical since their location in the weld geometry was slightly different; and hence, the beam impinged these holes by different angles. Moreover, the acoustic waves traveled along different paths with different lengths to reach the two holes at a fixed position of the wedge. This problem is normally rectified through implementing time gain compensation (TCG) curves, which can be obtained *via* incremental change of the probe distance relative to one of the SDHs and recording the gain difference needed to keep the signal amplitude steady. In the present study, a scan window was selected on the S-scan images to only cover the weld geometry by full-skip and 3rd half-skip beams. Then, the signal amplitude variations for one of the SDHs were simulated, as the SDH was moved to the extremities of the inspection window. The amplitude variations were

Table 1
Chemical composition of the parent plates, normal filler wire, and the hard-facing filler wire.

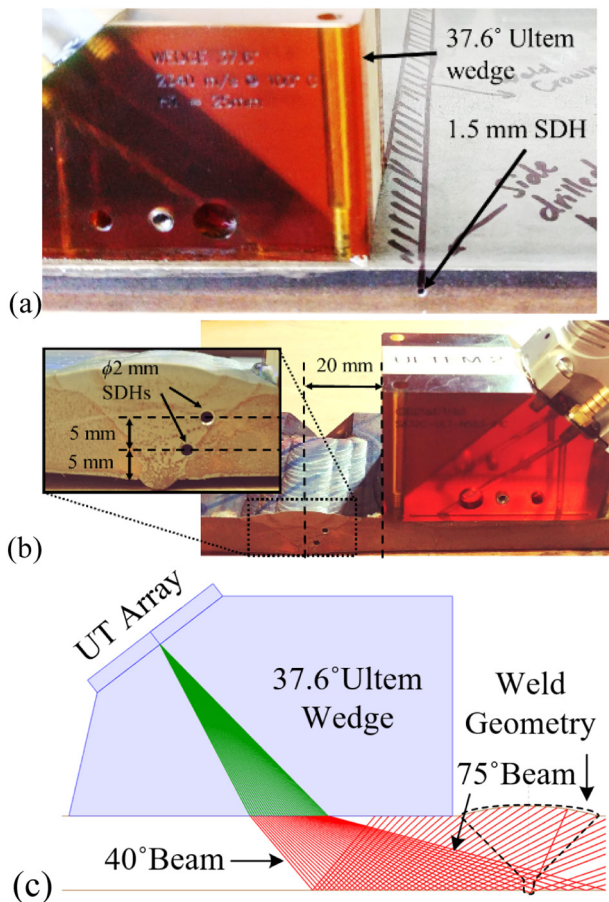|	Element wt. (%)				
	Cr	Mn	Si	C	Fe
S275	–	<1.5	<0.55	<0.18	Balance
Normal wire (SUPRAMIG)	9.5	0.5	3	0.08	Balance
Hard-facing filler wire	–	1.4	0.85	0.5	Balance

Fig. 4. Setup including the side-drilled holes for (a) primary, and (b) secondary calibrations, and (c) CIVA ray tracing verifying the coverage of the weld with the selected sweep angles.

Fig. 5. (a) the gain calibration based on the signal of the two $\phi 2$ mm side-drilled holes received in the S-scan image, (b) the adjustment of the horizontal position of the weld overlays with respect to the reflections received from the weld flanks in the S-scan image, and (c) the TOFD assembly of the transducers and wedges generating 70° compression waves within the weld.

measured to be negligible (less than ±1 dB) as compared to the signal amplitude of defects within the selected window; and thus, the TCG concept was not employed. To clarify these, the S-scan of the calibration holes and the scan window of interest marked by red is shown in Fig. 5 (a). A graphic representing the weld geometry was superimposed on the S-scan images. As depicted in Fig. 5(b), the position of these weld overlays was adjusted for each sample to fall over the reflections of the weld flank which were recorded at the unfilled weld groove present at the start and end of each sample.

All the samples were inspected along the weld-line, followed by the calibration procedure, and individual A-scans forming the S-scan image together were recorded at each position. The S-scan images presented in the next sections were normalized to the maximum amplitude of the indications obtained for calibration SDHs.

Moreover, TOFD inspections were also conducted to verify the observations of the sectorial scans. The instructions provided within BS EN ISO 10863 were followed to prepare the TOFD setup. Accordingly, two 10 MHz single element transducers were used for the purpose of transmitting and receiving. Each of them was mounted on a wedge generating 70° longitudinal waves inside the steel. The distance of the two wedges was adjusted to have the virtual focus of the two transducers at a depth equivalent to the two thirds of the parent plate thickness. This assembly is illustrated in Fig. 5(c).

The peak-to-peak amplitude for the lateral wave obtained by the TOFD system from each sample was set to the range of 40 to 80% of the screen height. An encoder was connected to the TOFD system to record the position data. The scan steps were chosen to be smaller than 0.5 mm to comply with standards. The TOFD assembly was scanned
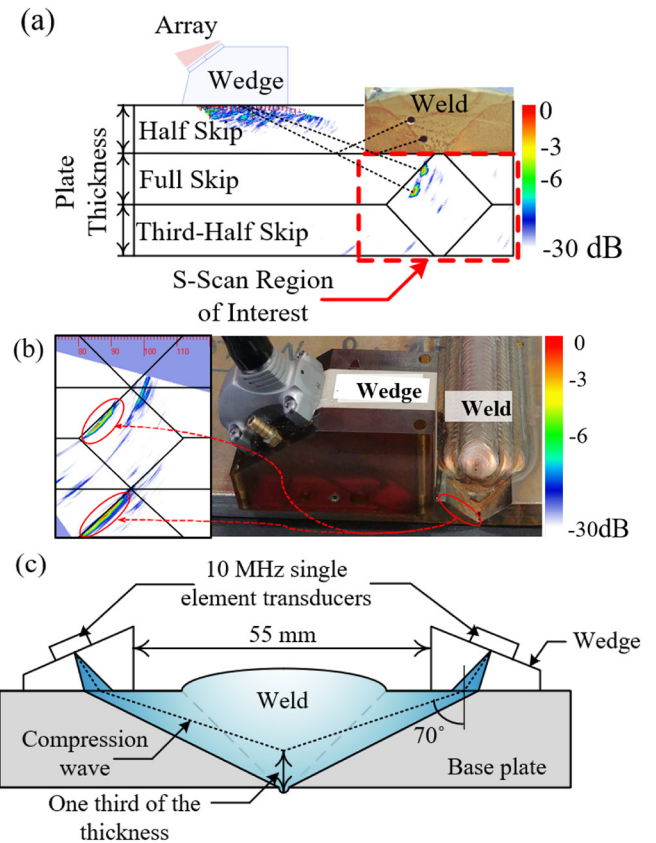
along the weld length; and consequently, a B-scan was formed using the encoded inspection data for each sample.

In TOFD images, the signals from a defect's upper and lower extremities are expected to appear as out of phase complementary wave marks on the A-scan as shown in Fig. 6. However, the upper tip of the defect in the TOFD scan of some samples may not be easily identifiable. This can be explained by the fact that the center of the weld body (*i.e.* the virtual focal point of the two TOFD transducers) is resolved better as compared to a zone closer to the weld crown because of the geometrical spread of
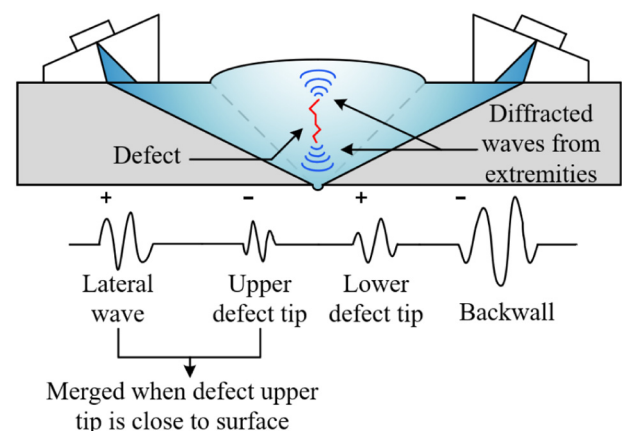

Fig. 6. Diffracted waves from the extremities of a defect in the weld and the expected phase of echoes in a TOFD A-scan.

Table 2
Description of the welded samples containing tungsten defects and their locations.

Sample ID	The process undertaken to create intentional defects	Defect location
T1	Tungsten rod ϕ 2.4 mm and length of 20 mm after pass 2 (layer 2)	Fig. 7(a)
T2	Tungsten tube with an inner diameter of 2 mm, an outer diameter of 3 mm, and a length of 30 mm embedded in weld after pass 9	Fig. 7(b)
T3	A vertical hole ϕ 3 mm and length of 9 mm is drilled in the weld after pass 11 (Layer 5) The hole is blocked by a ϕ 3 mm tungsten ball	Fig. 7(c)

the beam. Consequently, the signal from the upper tip of the discontinuity, if not already connected to the surface, merges with the lateral wave mark of the surface, and this results in the lateral wave to look weaker in amplitude. This was the case for some of the TOFD inspection results of the study.

3. Manufacturing welded samples with known-size embedded tungsten features

For the first series of samples, tungsten rod, ball, and tubes were embedded in specific passes during the welding (Table 2). The unique idea of using tungsten rods in the weld brings about the possibility of using them as known size calibration references. Therefore, sample T1 was manufactured with a rod placed in the weld after finishing the second layer. The tungsten rod was cut to a length of 20 mm and the extremities of it were ground flat. Afterward, a shallow slot was ground in the last layer to restrict its sideways movements as the arc pressure passed over it – see Fig. 7(a) and Fig. 8(a). The tungsten rod was then covered by subsequent weld passes. Using this methodology, it was possible to discover the extent that such a reflector could imitate the sound reflecting behavior of a linear-type weld defect such as an LoF. The
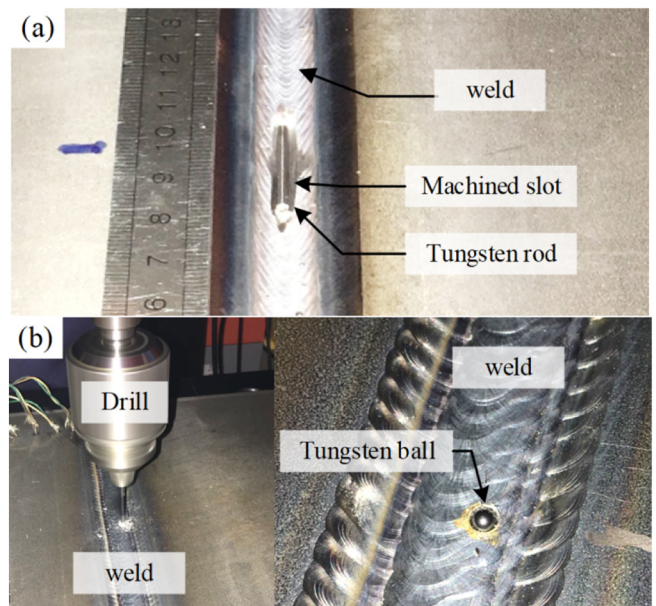

Fig. 8. (a) A shallow slot was ground in the weld after pass 2 and the tungsten rod was planted in the slot, and (b) a hole was drilled in the weld and a tungsten ball was placed on the mouth of the hole to block the flow of melt pool into the hole.

signal amplitude of a tungsten rod is expected to be smaller than that of an SDH due to the lower impedance mismatch of steel/tungsten as compared to steel/air. The percentage of ultrasound energy reflected at these interfaces were calculated according to Eq. (1), and using the wave velocity and density values that were either measured or adopted from the literature [35]. In this equation, Z_1 and Z_2 are the acoustic impedance of the first and second media, respectively. Almost 100% of a longitudinal ultrasound wave travelling in the steel will be reflected
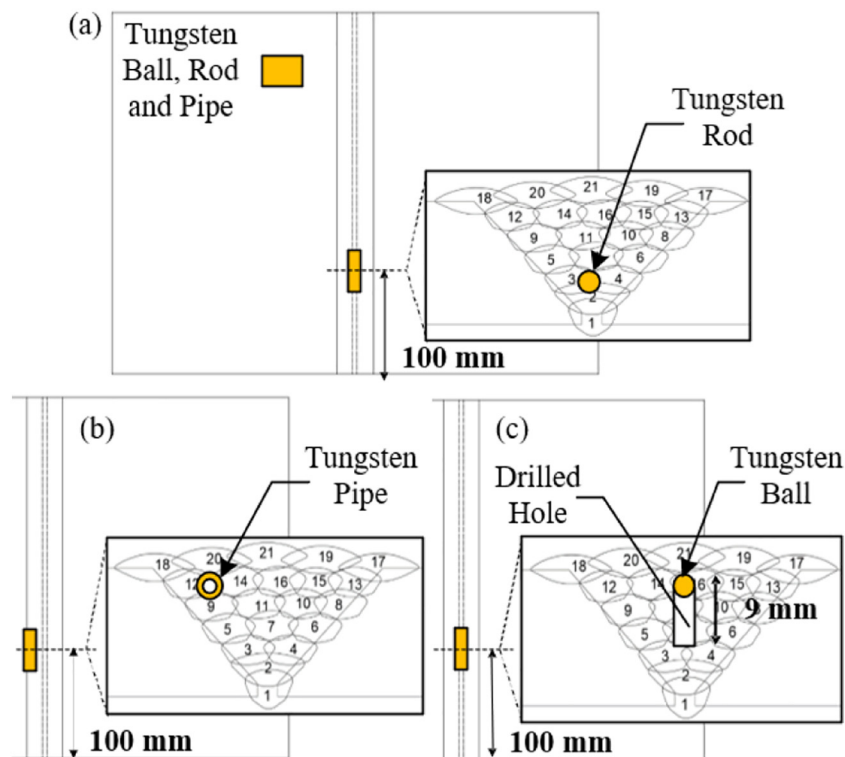

Fig. 7. The location and types of tungsten products embedded into the weld during the process for samples (a) T1, (b) T2, and (c) T3.

from the steel/air interface, where the steel is the first medium and air is the second, whereas this value is reduced to only ~13% at the interface of steel/tungsten.

$$R = \left[\frac{Z_2 - Z_1}{Z_2 + Z_1}\right]^2 \tag{1}$$

Bearing this in mind, a tungsten tube was embedded inside the weld of sample T2 to test the idea of generating a cylindrical air gap, as the possibility of incorporating such a defect during the welding process was very advantageous – see Fig. 7(b). The tube had a 2 mm inner diameter and a 3 mm outer diameter, and it was unlikely that the melt pool, which had a very high surface tension and low capillarity, could enter and fill the hole of the tungsten tube. The enclosed air gap within the tungsten tube was a better representation of an SDH.

Sample T3 was drilled after pass 11 to generate a vertical 3 mm diameter hole, as depicted in Fig. 7(c) and shown in Fig. 8(b). The opening of the hole was covered using a tungsten ball of the same size and it was expected that the cylindrical hole beneath the tungsten ball remained unfilled as the subsequent weld passes were deposited. The ball was used as a cap for the hole to stop the melt pool from entering the hole and result in an intended air gap forming below.

3.1. Ultrasonic inspections of manufactured welded samples with known-size embedded tungsten features

Fig. 9 summarizes the inspection results of the welded samples T1, T2, and T3 containing tungsten rod, tube, and ball, respectively. As demonstrated in the figure, the inspection results were provided in form of S-scan images for both sides of the weld. These S-scans were trimmed according to the size of the window shown in Fig. 9(a) where only the full skip and third-half skip results of the S-scan over the weld region were demonstrated. The color scale is the same for all the experimental sectorial scans across this manuscript where the 0 dB stands for the
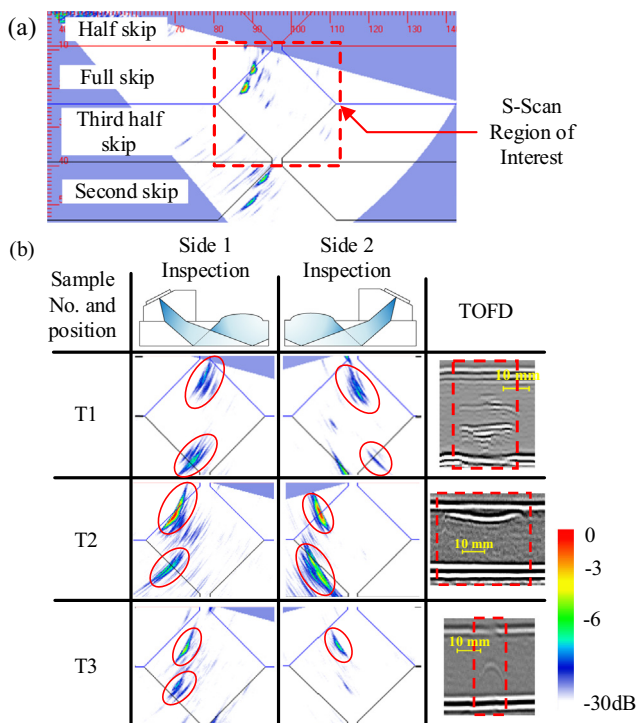

Fig. 9. (a) an example of the sectorial scan image, skip regions, and the region of interest extracted for the weld and, (b) the sectorial scan from sides 1 and 2 of the weld sections of T1, T2, and T3 samples alongside their TOFD scan results.

amplitude of the reference SDH hole. On the far-right side of Fig. 9(b), TOFD results were presented for the positions where an indication was observed. The TOFD image presented in the figure was cropped from the TOFD B-scan to only incorporate the lateral wave, defect indication, and backwall reflection.

The S-scans for the T1 sample showed that there were at least two very strong indications captured from each side of the weld. For instance, the inspection from side 1 had two indications received at the same horizontal position in the weld, with respect to the wedge position, but in two different skip regions. Hence, the indications were formed by two different beam angles that were reflected from the same feature in the weld. The feature was expected to be the tungsten rod. The scan from side 2 mainly had one strong signal captured in the full-skip region, and the signal presented in the 3rd half-skip region was significantly weaker from this side.

An explicit side view of the tungsten rod could be observed in the TOFD scan. The image contained the paired signals denoting the upper and lower tips of the defect in the weld. However, the signal from the lower side of the defect seemed to be slightly thicker (i.e. extended over time in the A-scans).

The S-scan and TOFD results for the inspection of sample T2 are illustrated in Fig. 9(b), where the inspections from both sides showed saturated signals captured by the full-skip beams. The TOFD image also showed the wave markings of the lower surface of the tube, however, there was no distinct indication received for the upper surface since it was placed in the weld after the final weld passes. It should be noted that the 3rd half-skip signals were approximately 5 dB lower in the amplitude, with reference to the calibration signal, and when the inspection was performed from side 2, the signal extended over a range of different angles (~10°).

The S-scan and the TOFD results related to sample T3 were also shown in Fig. 9(b) for the weld section where a tungsten ball was applied as a lid to a vertical hole to form an air gap. The S-scan image from side 1 shows two strong reflections happening at the same horizontal position in both full-skip and 3rd half-skip regions implying that the ball/hole was detected by 2 different S-scan angles. The reflection of the ball/hole was also visible in the full-skip region of the side 2 inspection images; however, the results suggested that the hole was very poorly captured by the 3rd half-skip beam. The maximum signal amplitude of these reflections was 5 dB lower than the calibration reference, which was comparable to the signal of the tungsten rod. The lower signal of such a hole, as compared to the calibration SDH, was certainly related to hole orientation relative to the incident beam direction since none of the swept angles in the S-scan was perpendicular to the hole's axis. Accordingly, the wave was majorly reflected from the hole conic corner and extremities. It was worth noting that the TOFD signal of the T3 sample, shown in Fig. 9(b), was very weak since the hole was drilled vertically and was only 3 mm in diameter. On a separate note, the orientation of the hole made the inspection very sensitive to the position of the wedge along the weld and the co-planarity of the array and the hole.

3.2. Destructive tests on manufactured welded samples with known-size embedded tungsten features

To verify the source of indications received in the inspection results of samples T1 to T3, a section from each welded sample was extracted using a waterjet as shown in Fig. 10. The cut surface passed through the position where the defect signal was observed. Then, the surface was polished and etched using a mixture of nitric acid and deionized water as the etchant solution.

A macrograph of the inspected section of sample T1 is presented in Fig. 10 to gain a better understanding of the inspection results. The tungsten rod had a very tight fusion boundary with the weld material (i.e. there was no visible separation between the tungsten rod and the steel substrate at the macrograph section). However, there was a lack
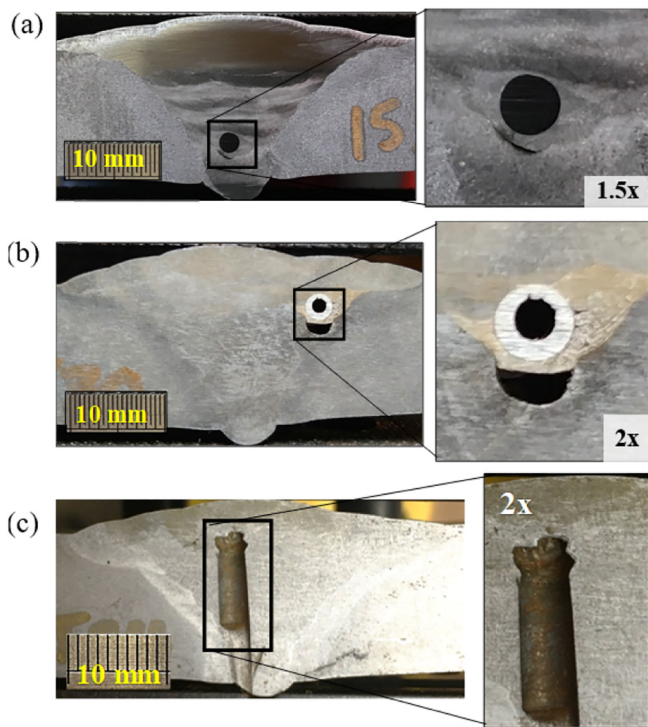
Fig. 10. The macrograph sections of welded samples (a)T1 with a ϕ 2.4 mm tungsten rod, (b) T2 containing a tungsten tube with an inner diameter of 2 mm, and (c)T3 with a vertically drilled ϕ 3 mm hole.

of fusion defect just beneath the rod, positioned a few millimeters apart from the rod's surface. The LoF at this location was associated with the slot that was machined in the weld to place the rod inside. The fabricated slot might have been slightly deeper than desired since the machining was carried out manually, and there was a lack of control on the size. Due to this fact, an air gap remained underneath the tungsten rod. Thus, when the next weld bead was deposited, the lack of mobility of the melt pool and its high viscosity could have inhibited the melt from filling the air gap beneath the tungsten completely. This LoF defect which was occurred beneath the tungsten rod explained the stronger signal of the lower surface of the rod received in the TOFD image – see Fig. 9(b).

The inspected section of the T2 weld was also cut open and the tungsten tube embedded in the weld was revealed in Fig. 10(b). The figure showed that the tungsten tube had good peripheral bonding with the substrate however, there was a semi-elliptical LoF defect located just below the tungsten tube with its major axis equal to the outer diameter of the tube (3 mm). This LoF defect was situated where the slot was fabricated to place the tube in the weld.

Following the same rationale used for explaining the LoF defect under the tungsten rod, this large defect could also be correlated to the melt pool was not able to penetrate fully into the slot. The position of this large LoF defect also explained the saturated echoes received in the full-skip inspection since the beam firstly hit the LoF before reaching the tube. The 3 mm LoF closely emulated a 3 mm SDH with a stronger signal than the calibration reference of 2 mm SDH, leading to a saturated indication. On the other hand, the 3rd half-skip signal of the T2 sample inspected from side 1 had a 3 dB lower amplitude relative to the calibration SDH. This was related to the beam reaching the tube from the top where the LoF was not present. Accordingly, the amplitude of this signal could be associated with a Ø 2 mm hole within a tungsten rod of Ø 3 mm, assuming that no melt has entered the tube. This was testimony to the effectiveness of the tungsten tube as an intentional defect since it could be used in-process to build a calibration reference very similar to the SDHs that could be drilled only in the finished welds.

T3 weld was also cut open from the position where the inspection was performed. It was found that the drilled hole was properly blocked by the tungsten ball in a way that the drilled hole remained intact in the weld. Therefore, the strong reflections in the S-scan of sample T3 could be linked to this vertical hole.

3.3. Ultrasonic simulation of manufactured welded samples with known-size embedded tungsten features

To better understand the indications provided in Fig. 9(b), a PAUT inspection model of the weld was prepared in CIVA. The CIVA workspace only allows for 3-dimensional (3-D) models to be generated however, these models can be computed using 2-dimensional (2-D) approximation to minimize the solver time if the geometry of the transducer and the sample, including the defects, are invariant in the 3rd dimension. This is the case for the samples T1 and T2, where a tungsten rod/tube is extended along the weld length and their length exceeds the array's elevation. Noteworthy that due to the semi-analytical formulations of the CIVA solver, the software only allows for limited predefined flaw geometry to be modeled. Therefore, it was not possible to model the flaws in T2 and T3 samples.

The parameters related to the phased array probe and the high-temperature ULTEM™ wedge were assigned to the model assembly domains. The wedge offset from the center of the groove was adjusted according to the distance of 20 mm measured in the inspection setup. The wedge and the base plate velocities, which were either extracted from datasheets or measured using experiments, were assigned to the model domains. Adhering to the experimental calibration process, initially, the S-scan for the 2 mm SDHs of the calibration specimen was simulated in CIVA and the maximum amplitude of the SDH signals was taken as the calibration reference. This value was later used as a fixed calibration across the CIVA simulations to normalize the amplitudes.

CIVA model of the T1 sample was prepared in 3-D comparable to the macrograph of Fig. 10(a). The tungsten was modeled by a cylindrical inclusion extending for 20 mm in the weld direction. Similarly, following the LoF profiles of Fig. 10(a), the curved profile below the tungsten inclusion was also sketched and extruded for the length of 20 mm into the welded section and then, the models were run with 2-D approximation.

3.4. Comparison of simulated and experimental inspection of manufactured welded samples with known-size embedded tungsten features

The S-scan images obtained from the modelling and experiments collected from sides 1 and 2 of the weld section of sample T1 were compared in Fig. 11. The S-scan modeled for the inspection from side 1 outlined the nature of the repeated indication that was observed for the full-skip inspection of the tungsten rod. According to the full-skip simulation results shown in Fig. 11(a), one strong echo which was a combined echo of the LoF and the substrate/tungsten boundary appeared before the tungsten. Besides, two weaker echoes were received after the tungsten with the first one from the tungsten/substrate and the latter was a reverberation of the first. In the full-skip results acquired from side 2 and presented in Fig. 11(b), the primary echo was 2 dB weaker as compared to the side 1 signal because of the LoF defect located on the left (far) side of the tungsten. Although the difference was not as evident in the experimental S-scans, the overall matching of the maximum simulated amplitude of tungsten with the experimental case was very good.

The 3rd half-skip indication was only received on side 1 inspection where the estimated signal amplitude was 10 dB lower than that of the measured one. The geometries of the tungsten and the LoF were extended uniformly in the length of the weld inside the model whereas their actual geometries in the third dimension were unknown except at the macrograph surface. This could contribute to the amplitude
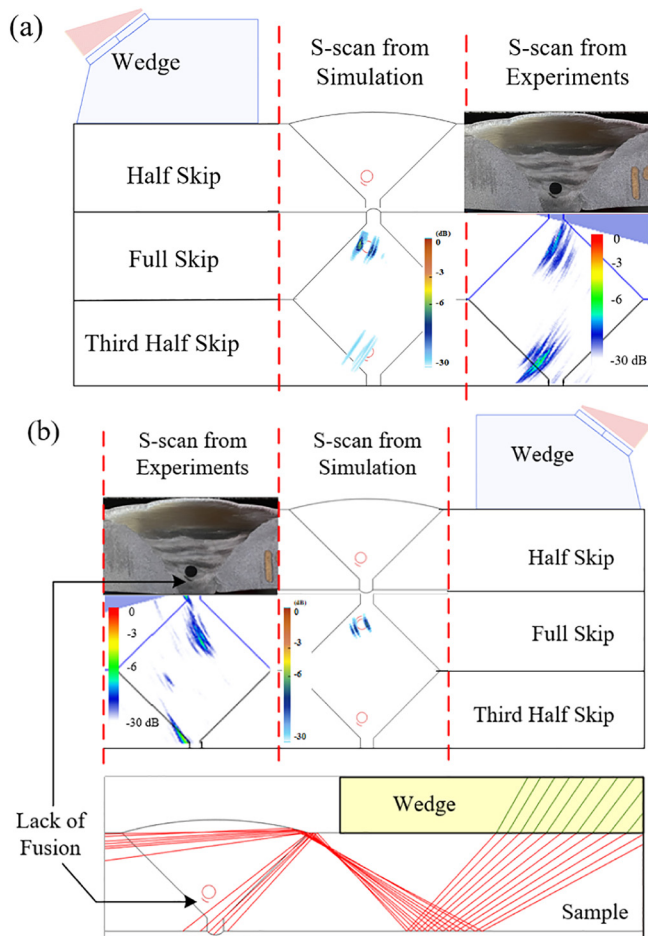
Fig. 11. CIVA simulated and experimentally recorded S-scans of the T1 welded sample containing a tungsten rod and a lack of fusion when the weld section is inspected from sides (a) 1 and (b) 2.

Fig. 12. (a) Simulated inspection of a 2 mm SDH placed in the weld. The hole position was set following the location of the tungsten tube in sample T2, (b) Experimental inspection results for the tungsten tube in sample T2, (c) A 51° beam tracing as it hit the SDH, indicating the start of the prolonged indication in the 3rd half-skip, and (d) A 60° beam tracing as it hit the SDH, indicating the end of the prolonged indication.

Table 3
Description of the welded samples, their intentional defects, and the location of intentional defects.

Sample ID	The process undertaken to create intentional defects	Defect location
Q1	• Position 1: Localized water quenching for a length of 30 mm on the weld after pass 7 (layer 4) • Position 2: High temperature paste for a length of 30 mm on the weld after pass 7 (layer 4)	Fig. 13(a)
Q2	• Quenching after deposition of each layer of the weld • Immersed in a water tank right after finishing the weld for 60 h	Fig. 13(b)
Q3	Localized quenching after pass 9 (layer 5) for a length of 40 mm	Fig. 13(c)

differences observed between the model and the experiment. As depicted at the bottom of Fig. 11(b), the beams must bounce from the weld crown to reach the tungsten in the 3rd half-skip; therefore, they were scattered following this path, and no signal was received. This was provided in support of the experimental S-scan observations.

To investigate the reason causing the extended indication of the T2 sample in the S-scan image which was discussed in Fig. 9(b), a 3-D model of the weld containing a Ø 2 mm SDH was prepared in CIVA and the weld was inspected from side 2. As demonstrated in Fig. 12(a), the prolonged simulated signal was comparable to the experimental one in Fig. 12(b). To explain the observation, the 3rd half-skip beam bounced from the weld cap before reaching the SDH, and, owing to the concavity of the cap, the beam impinged the SDH starting from the angle 51° up to 60° as depicted in Fig. 12(c) and (d).

4. Manufacturing of welded samples with intentional defects – cracks using water quenching

Three weld samples were prepared using the welding system. Different quenching strategies were tested for samples Q1, Q2, and Q3 to check the feasibility of creating controlled weld cracks. Table 3 lists the samples and summarizes the processes adopted to introduce weld defects in each of them. A combination of factors, such as post-weld residual stresses and hydrogen concentration, could increase the chance of forming such cracks [32]. Samples Q1 and Q3 were both quenched locally (i.e. on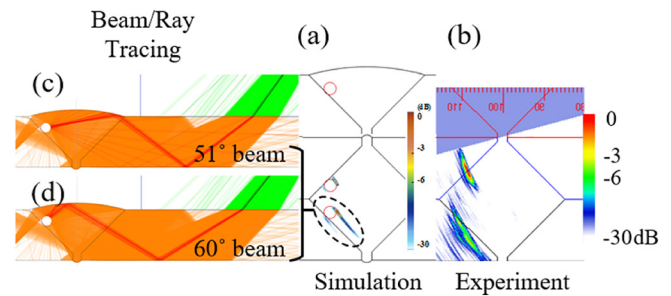ly on a part of the weld surface) by spraying water onto the weld surface directly after deposition of the 4th and 5th layers of the weld, respectively.

For localized quenching, the weld was covered with a high-temperature insulation blanket, which was also a liquid absorbent material, and the cover was only cut open for the area of interest. Therefore, only a small area of the weld surface was exposed to the water spray while the blanket conserved the sample heat. Moreover, some high-temperature paste was embedded in the weld at position 2 of the Q1 sample to produce inclusion defects. However, the weld section of sample Q2 was entirely quenched after the deposition of each layer and the manufactured sample was completely submerged in a water tank for 60 h immediately after finishing the weld.

4.1. Ultrasonic inspections of manufactured welded samples with intentional defects- cracks

Fig. 14 depicts the inspection results of sample Q1 at two scanning positions. The first row of Fig. 14 shows that a relatively strong indication with an amplitude of −6 dB was captured by the full skip of a 70 degrees beam when the weld was inspected from side 1. The same feature could not be identified in the full-skip region of the image when the weld was inspected from side 2; however, an indication with an amplitude of −10 dB was visible in the third half-skip from side 2. The lower amplitude of side 2 indication originated from the higher Time of Flight (ToF) of the 3rd half-skip beam and its different incident angle to the reflector.

The TOFD image presenting the inspection result of the Q1 weld geometry in position 1 shows a black and white watermark signal coming from the lower tip of the flaw whereas the signal from the upper tip of the flaw was merged with the lateral wave resulting in a weaker surface indication.

The S-scan images for the inspection position 2, as marked in Fig. 13 (a) of the Q1 sample, were presented in the second row of Fig. 14. The
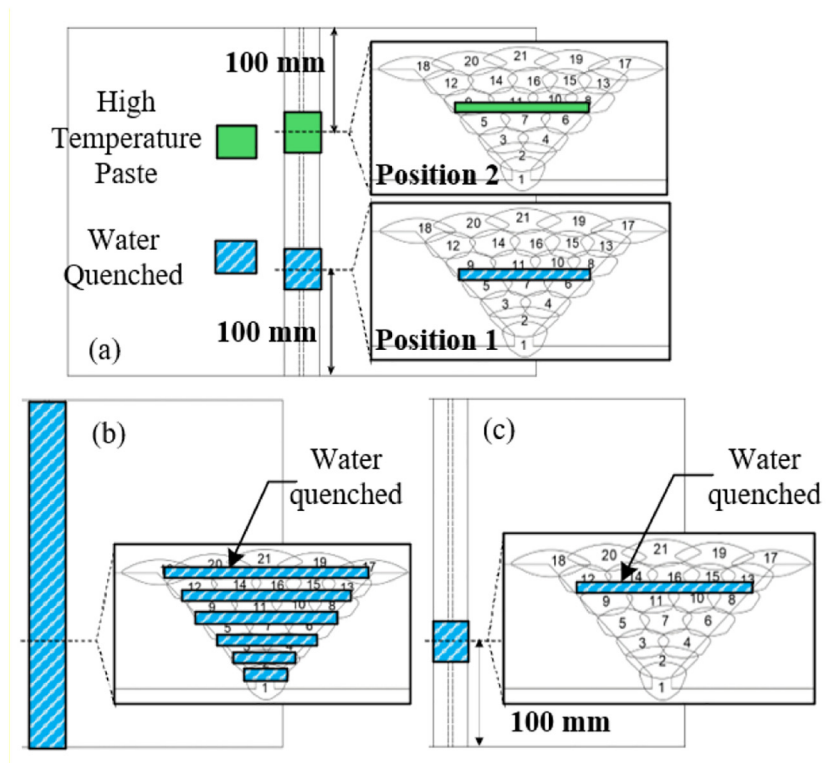
Fig. 13. The location and types of defects introduced to the weld during the process for samples (a) Q1, (b) Q2, and (c) Q3.

small indications marked in this figure, when the inspections were conducted from sides 1 and 2, was at least 9 dB lower in amplitude as compared to the indication of the defect detected at position 1. Despite the very low amplitude of around −15 dB, the indications are still above the noise level.

Shown in Fig. 15 are the inspection results of samples Q2 and Q3. According to the S-scans in the first row of the figure, a strong indication was captured by the full-skip beam. The indication was very close to the weld center and it stood out in the images of sample Q2. The signal amplitudes received for this feature, when inspected from either side of the weld, were at the same level as the amplitude obtained for the defect of the Q1 sample at position 1. Two individual wave mark indications could also be spotted in the TOFD image. These wave marks were received at different depths within the weld. The signals indicated the tip of a defect inside the weld; however, like the previous sample, they did not appear in complementary pairs.

The blurry section of the lateral wave occurring just above the crack's signal and the missing leg of the pair for the crack's tip signals in the TOFD image implied that the flaw was extended to the vicinity of the top surface.

Regarding the S-scan of the Q3 sample in Fig. 15, a series of discrete indications in the middle of the weld could be observed from either side. In the TOFD image of the same sample, only the lower tip of a defect was signified by strong positive and negative wave marks. Furthermore, the lateral wave was faint in this section, similar to the inspection results presented for the two samples Q1 and Q2. The wave marks of the crack appeared to extend up to the extremity of the weld, representing a long crack that spanned over 20 mm of the weld length. The highest signal amplitude for this crack was recorded from the side 1 inspection using a 3rd half-skip beam. However, the amplitude is 2 dB lower than the maximum signal amplitudes recorded for the 2 previous cracks found in samples Q1 and Q2.
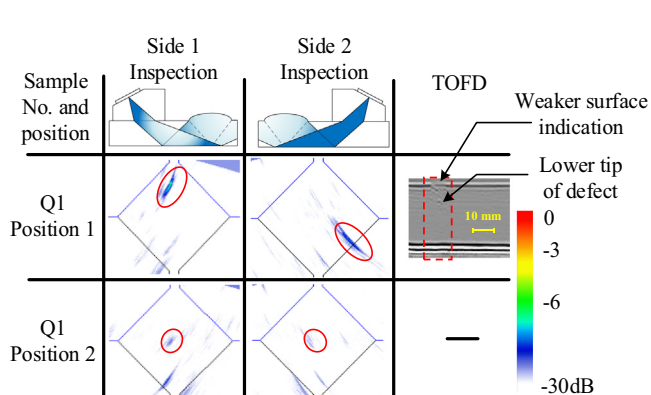

Fig. 14. the sectorial scans from sides 1 and 2 of the weld section of Q1 sample at two different positions together with the results of TOFD.
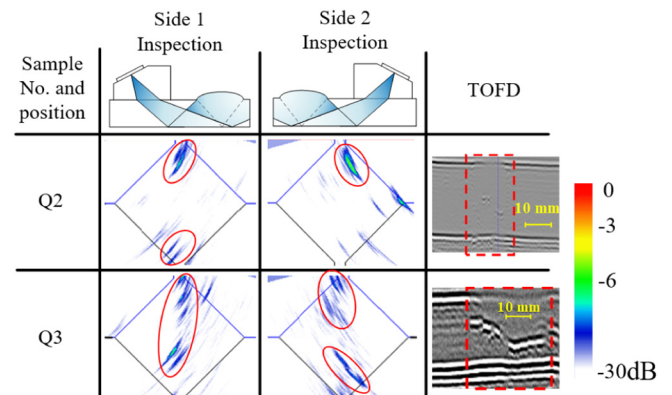

Fig. 15. the sectorial scan from sides 1 and 2 of the weld sections of Q2 and Q3 samples together with the TOFD results.

Since the signal amplitude of the tungsten rod presented in Section 3 was comparable to the signal amplitude of the cracks presented here, it could be concluded that the inclusion of a tungsten rod in the weld is not a viable method for replicating an SDH. However, this makes it a better reference for gain calibration and possibly sizing, when crack detection is desired.

4.2. Destructive tests on manufactured welded samples with intentional defects- cracks

The macrograph of sample Q1 at inspection positions 1 and 2, presented in the image of Fig. 16(a), revealed two cracks at this section, where (I) a larger one, marked by number 1, propagated from the quenched area and extended to the weld root, and (II) a second, smaller crack, labeled by 2, started from the quenched area and extended toward the fusion boundary between the weld and HAZ. The figure proved that both cracks had been initiated from the area at which the localized water quenching was performed (*i.e.* after pass 7). This stood for the effectiveness of water quenching. It was also interesting to see that the crack growth was stopped at the boundary of the weld and the HAZ. This occurred since the parent material and the HAZ had higher ductility in comparison with the brittle weld region which was deposited using the hard-facing wire.

A microscopic image of this etched surface was superimposed on the S-scans captured from both sides of the weld in Fig. 16(b). The acoustic paths of the beams that provided the largest indication of the cracks were also sketched on the figure by red dashed lines. As can be seen, the acoustic path of the beam indicating crack 1 from side 1 was bounced from the plate back wall and hit the lower part of the crack (*i.e.* closer to the root). This part of the crack was orientated in a manner that the full-skip beam provided a specular reflection of the crack. It

should be noted that the acoustic beam did not reach crack 2 as it was masked by crack 1. However, when the inspection was done from side 2, an indication of crack 2 was received in the 3rd half-skip region. As demonstrated in the figure, the beam bounced twice from the back and the top surfaces and then impinged the face of the crack.

The polished and etched section of the weld at position 2 of sample Q1, illustrated in Fig. 16(a), shows a porosity colony that originated from the residue of the high-temperature paste. The mean size of the pores which measured to be approximately 0.1 mm was smaller than the UT detection limit determined by $\lambda/2$ (0.3 mm), as a rule of thumb. However, these porosities were partly coalesced and formed a lattice with a size of a few millimeters in some parts. Therefore, the signal received at this position could be either attributed to the porosity colony or another feature that was not revealed in the polished section and yet might have been captured at this testing position. Accordingly, it was not conclusive whether the high-temperature paste could act as a defect inducing agent.

The Q2 sample was cut at the inspection position and then polished. The resulting surface is depicted in Fig. 17(a) after etching where an almost straight crack was vertically extended in the weld geometry. The crack provided a very clear indication in the S-scan image of Fig. 15, showing a stronger amplitude from side 2. The crack profile at the etched surface was slightly curved with its concavity toward the side 2 inspection, which resulted in stronger signal amplitude. The nature of this crack was believed to be different from those discussed earlier for sample Q1 since this crack was less branched and its profile was less curved. Furthermore, the crack of Fig. 17(a) started from the middle of the weld and did not connect to any boundaries, unlike those found in the Q1 sample. The beam tracing of the Q2 sample was plotted on the sectorial scan image and the weld overlays as shown in Fig. 17(c). From the TOFD results, it was expected that the crack profile extended
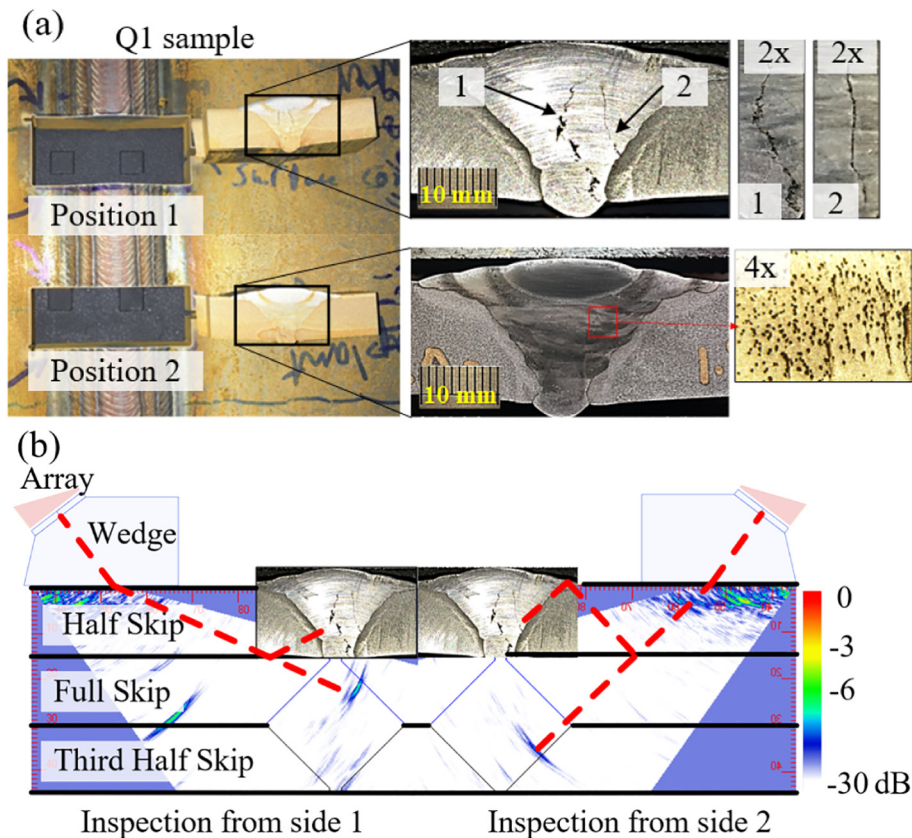

Fig. 16. (a) Macrograph samples extracted at positions 1 and 2 from the welded section of Q1 sample. Two visible cracks at the etched surface of Q1 at position 1 and a porous region of the weld observed at the etched surface of Q1 at position 2. (b) Beam tracing on the S-scan image for the inspection of the two cracks of sample Q1 at position 1 from sides one and two.
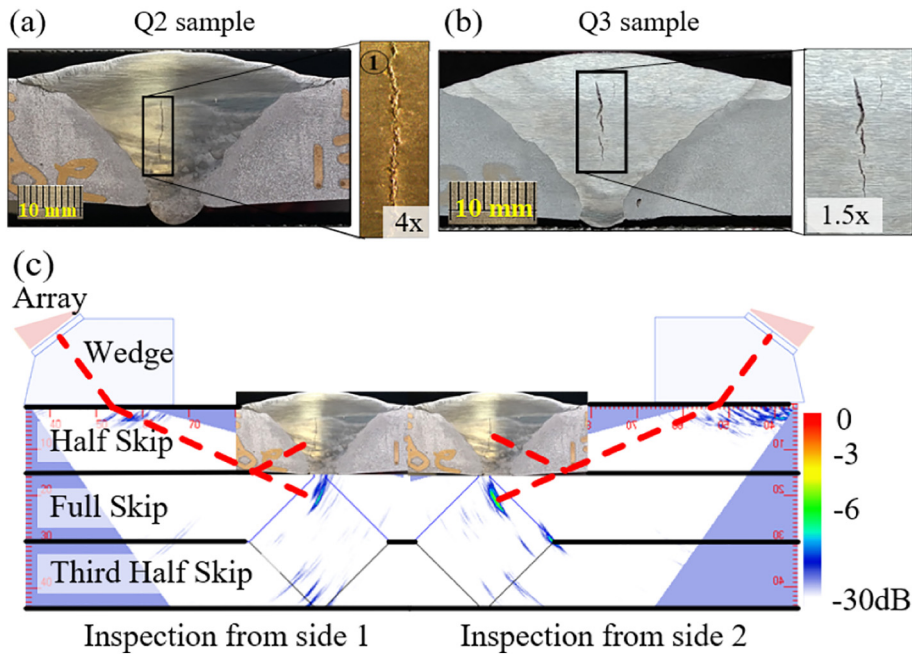
Fig. 17. A macrograph sample cut from the welded section of (a) Q2 and (b) Q3 samples including successfully induced cracks. (c) Beam tracing to the strongest indications of the S-scan image acquired at the location of the crack for Q2 sample.

very close to the weld crown, however, the etched section did not suggest this. As mentioned before, this was attributed to the low resolution of the TOFD for the top portion of the weld.

The macrograph of the weld section Q3, presented in Fig. 17(b), helped understand the disjointed and complex indication seen in the S-Scan image of Fig. 15. As can be seen the broken profile of the crack propagated in small sections, vertically through the middle of the weld geometry. The lower signal amplitude of this crack, as compared to the other two, could be explained by the disconnected crack profile.

4.3. Ultrasonic simulation of manufactured welded samples with intentional defects - cracks

The crack profiles in the macrograph of the weld section in Fig. 16 (a) were reproduced using a 2-D CAD profile within CIVA. The profiles were extruded along the weld length for 10 mm to generate planar defects. Afterward, an S-scan of 40° to 75° with an angle step of 1° was modeled. A maximum number of 4 half-skips (2 skips) was selected for the solver to avoid lengthy computations. The S-scan results were normalized by the calibration amplitude. Afterward, the results were superimposed on the weld and the crack layouts to assist the understanding of echoes as shown in Fig. 18.

4.4. Comparison of simulated and experimental inspection of manufactured welded samples with intentional defect - cracks

The comparison between the S-scan image generated by CIVA and the image obtained in the experiments when the scan was carried out from side 1 on the Q1 sample is provided in Fig. 18(a). The position of the crack signal inside the weld predicted by simulation agreed well with the actual position of the signal. The simulation also confirmed the beam tracing of Fig. 16(b) where the strongest reflection was captured from crack 1 *via* the full-skip beams whereas, crack 2 was masked by crack 1, and no indication was received for it on the S-scan. Even though the actual crack extension in the third dimension (*i.e.* perpendicular to the weld section) could be significantly different from the assumption of a planar defect in this model, the simulated signal amplitude supports the experimental measurements.

Fig. 18(b) presents the simulated and experimental S-scans for the same defects inspected from side 2 of the Q1 weld. As suggested by the beam tracing of Fig. 16(b), the indication with the highest amplitude appeared in the 3rd half-skip region when the inspection was done
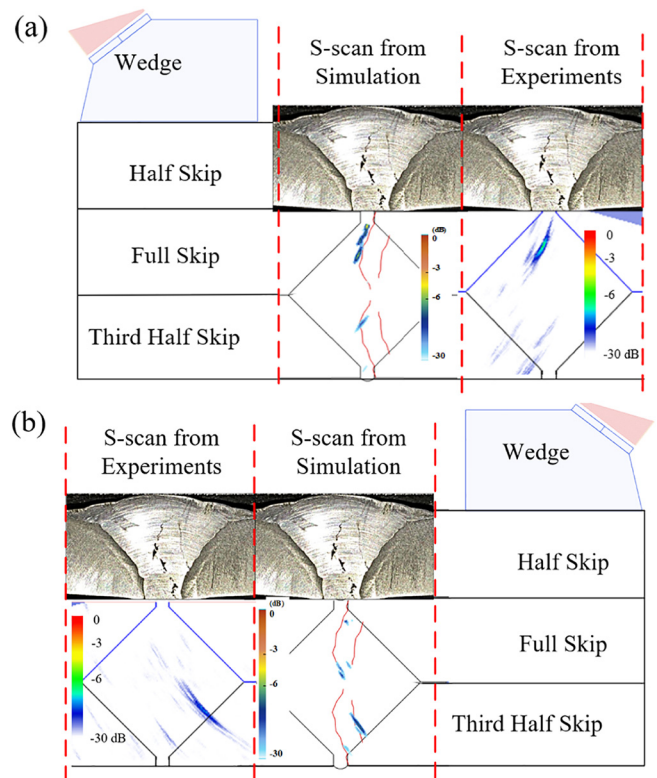

Fig. 18. A comparison between the CIVA simulations and experimentally recorded S-scans of the Q1 welded sample at position 1 with two multi-faceted cracks. Inspections are conducted from sides (a) 1 and (b) 2.
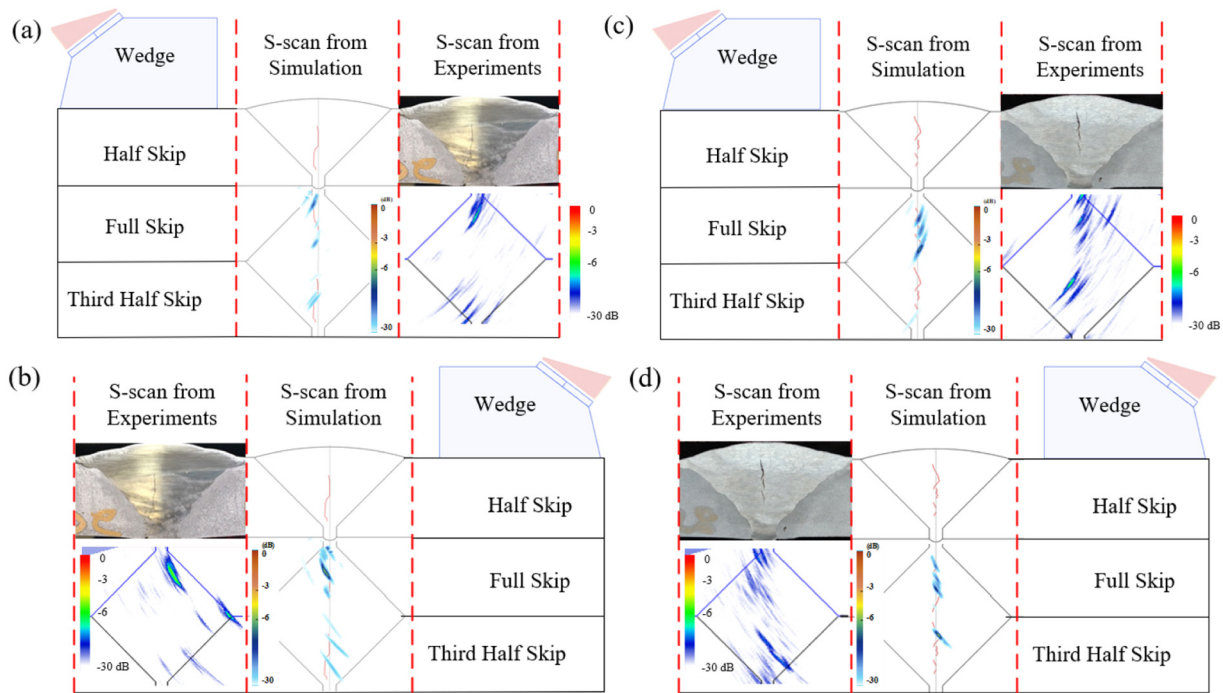
Fig. 19. A comparison between the simulated and experimental S-scans of the Q2 sample form sides (a) 1 and (b) 2, and the Q3 sample form sides (c) 1 and (d) 2.

Table 4
Measured and modeled amplitudes of the artificial defects embedded in the welds. All the presented amplitude values are relative to the calibration amplitude.

	Max Amplitude (dB)	Model-Based Estimation (dB)		Max Amplitude (dB)	Model-Based Estimation (dB)
Rod (T1)	−6	−6	Crack (Q1)	−6	−6
Tube (T2)	0	–	Crack (Q2)	−6	−6
Ball (T3)	−5	–	Crack (Q3)	−8	−9

from side 2. A closer look at the simulated S-scan of Fig. 18(b), and the beam tracing in Fig. 16(b), implies that the indication corresponded to crack 2 where the 3rd half skip beam impinged the crack profile perpendicularly. The simulated S-scan was following the experimental one in terms of the angle, ToF, and the amplitude of the indication.

The CIVA simulation results for the scan of sample Q2 from side 1 and 2 are compared with the S-scan images in Fig. 19(a) and (b), respectively. Simulations showed a stronger reflection from side 2 of the crack in the full-skip image. The simulated defect amplitudes were comparable to those acquired for the crack in the experiment, while the location of the strongest simulated indications matched the notable indications in the experimental S-scan images.

Sample Q3 and its ridged crack with discrete sections were also modeled, and the simulated and measured inspection results were compared in Fig. 19(c) and (d). A series of indications were observed from either side of the rough crack profile in both simulations and experiments, with a high degree of agreement between them. The crack profile of sample Q3 is very difficult to mimic within the software; hence, in these figures, it can be seen the simulated indications are slightly displaced as compared to those in the S-Scan images of sides 1 and 2. However, the amplitudes were found to be in good agreement.

5. Conclusions

Calibration and verification of automated In-Process NDT systems are critical to ensuring optimum product and process integrity. This paper presented the results of a study investigating the simulation, manufacture, experimental inspection, and verification of calibration techniques and procedures for intentional weld defects that form the basis of a quantitative approach to in-process weld inspection.

A number of components were welded using an integrated system comprised of a robot and different sensors carrying out multi-pass automated deposition. Two different intentional defect inducing strategies were tested during the manufacturing of the weld, notably known size tungsten features and induced cracking. PAUT shear wave S-scans and TOFD inspections were conducted on the manufactured weld sections containing deliberate defects and the inspection results were presented in form of S-scan and TOFD B-scans images. The experimental observations were also verified through macrographic destructive tests, and the CIVA ultrasonic simulations were carried out for a better understanding of wave propagation, inspection skips, and UT wave interaction with the generated defects. The measured and model-based estimation of the maximum S-scan signal amplitudes are summarized in Table 4, where a close agreement between the simulated and measured amplitude values was yielded.

The following was concluded from the study:

1. A technique to introduce artificial lack of fusion weld defects by the inclusion of three different types of tungsten inclusions was proposed. It is observed that:

   - Embedding a tungsten rod in the weld was not deemed successful in simulating the signal of a reference SDH for calibration purposes since it had a repeated signal in the S-scan image, where the first signal was related to the reflection from substrate/tungsten and the second one was attributed to the tungsten/substrate. The other difference was the amplitude of the signal of the tungsten being 6 dB

lower than the reference SDH. Provided the scale of the signal amplitudes of the cracks witnessed in this study, the tungsten rod could be considered as a reference for gain calibration for detecting realistic cracks.

- The tungsten tube planted in the weld with an inner diameter of 2 mm produced signals 3 dB lower in amplitude when compared to the signal of a 2 mm SDH. The tube was extended over a section of the weld enabling the repeatability of the in-process inspection and it produced an amplitude level which was 3 dB higher than the signal amplitude of the cracks inspected here. Other sizes of tubes with different internal diameters could be used to tailor the reference amplitude to fit the sizing application and the acceptance criteria. Further studies are needed to tackle the challenge of planting the tube in the weld, so the surrounding of the tube is properly filled with the molten material.
- The tungsten ball covering a vertically drilled hole also produces the same signal amplitude that was received for the rod. This defect was very localized, and accordingly, the signal amplitude was very sensitive to small changes in the placement of the wedge with respect to the defect. Therefore, the nature of the defect could result in repeatability challenges when used for calibration.

2. A technique was proposed for creating artificial cracks using water quenching into the weld geometry to simulate the real cracking scenarios and the following were observed:

- Ultrasonic inspection and simulation of weld sample Q1 with two large cracks showed that one of the cracks could mask the other and adversely affect the detectability of the weld cracks if the inspection was performed from one side. Therefore, if a robotic in-process inspection was to be carried out, which is the topic of a larger project supporting this work, it is strongly recommended to use a tandem array configuration on both sides of the weld or to conduct a repeated inspection from both sides, which is common practice in manual phased array inspections.
- Localized quenching of the weld, which was performed during the manufacturing of samples Q1 and Q3, was successful in creating cracks starting from the layer on which the quenching was carried out. The amplitude of these cracks was 6 dB lower than the calibration amplitude and these observations were successfully supported by CIVA simulations.
- The second quenching strategy used in sample Q2 was also successful in generating the crack in the weld section, however, the control on the location of the crack was very low since all the layers were subjected to quenching. Also, it was observed that the crack was slightly different from the other samples having fewer facets and branches. Further investigations could be conducted to classify these cracks. The amplitude level of the signal obtained for this crack was on the scale of the two others.

A range of methodologies was introduced in this research for embedding tungsten in the weld and quenching the weld to generate artificial cracks. These approaches are instrumental in understanding: a) the effect of defect morphology and orientation on signal amplitude, b) the phased array instrument gain levels required for detection of weld cracks in the present case, c) how to substitute SDHs with embedded tungsten defects to tackle high-temperature in-process calibration of instrument gain for PAUT inspection, d) how to create quenching-induced cracks that can be used to train practitioners, and to study the signal amplitudes and indication locations of common weld defects.

Credit author statement

Ehsan Mohseni: Conceptualization; Data curation; Investigation; Formal analysis; Writing - original draft; Writing – review & editing.

Yashar Javadi: Conceptualization; Methodology; Investigation; Supervision; Data curation.

Nina E. Sweeney: Methodology; Writing - review & editing.

David Lines: Software; Writing – review & editing.

Charles N. MacLeod: Funding acquisition; Project administration; Supervision; Resources; Writing – review & editing.

Randika K. W. Vithanage: Data Curation; Investigation; Visualization.

Momchil Vasilev: Software; Investigation.

Zhen Qiu: Conceptualization; Formal analysis.

Carmelo Mineo: Software; Writing – review & editing.

Peter Lukacs: Software.

Euan Foster: Data curation; Writing – review & editing.

S. Gareth Pierce: Funding acquisition; Project administration; Resources; Writing – review & editing.

Anthony Gachagan: Funding acquisition; Project administration; Resources.

Declaration of Competing Interest

The authors declare that they have no known competing financial interests or personal relationships that could have appeared to influence the work reported in this paper.

Acknowledgments

References

[1] D. Radaj, Design and Analysis of Fatigue Resistant Welded Structures, Elsevier, 1990.
[2] W. Fricke, Fatigue analysis of welded joints: state of development, Mar. Struct. 16 (3) (2003) 185–200.
[3] J. Sun, et al., Study on the weldability, microstructure and mechanical properties of thick Inconel 617 plate using narrow gap laser welding method, Mater. Des. 175 (2019) 107823.
[4] J. Rogerson, Defects in welds: Their prevention and their significance, Quality Assurance of Welded Construction, CRC Press 1983, pp. 129–144.
[5] R. Halmshaw, Introduction to the Non-Destructive Testing of Welded Joints, Woodhead Publishing, 1996.
[6] B.S. Institution, BS EN ISO 17640: 2018, Non-destructive testing of welds, Ultrasonic Testing. Techniques, Testing Levels, and Assessment 2019, p. 40.
[7] B.S. Institution, BS EN ISO 19285: 2017, Non-destructive testing of welds, Phased Array Ultrasonic Testing (PAUT). Acceptance Levels 2017, p. 30.
[8] D.E. Bray, R.K. Stanley, Nondestructive Evaluation: A Tool in Design, Manufacturing and Service, CRC Press, 1996.
[9] Y. Javadi, et al., In-process calibration of a non-destructive testing system used for in-process inspection of multi-pass welding, Mater. Des. (2020) 108981.
[10] M. Consonni, C.F. Wee, C. Schneider, Manufacturing of welded joints with realistic defects, Insight-Non-Destruct. Test. Cond. Monit. 54 (2) (2012) 76–81.
[11] M. Marvasti, et al., Phased array inspection at elevated temperatures: effects of ultrasonic beam skew, Insight-Non-Destruct. Test. Cond. Monit. 56 (5) (2014) 256–263.
[12] M.H. Marvasti, A.N. Sinclair, Phased array inspection at elevated temperatures, 2014 IEEE International Ultrasonics Symposium, IEEE, 2014.
[13] Zhen Qiu, et al., Study of thermal gradient effect for in-process ultrasonic inspection of fusion welding, 2019 IEEE International Ultrasonics Symposium (IUS), 2019 , Glasgow, UK.
[14] Y. Javadi, et al., Continuous monitoring of an intentionally-manufactured crack using an automated welding and in-process inspection system, Mater. Des. (2020) 108655.
[15] R. Bogue, The role of robotics in non-destructive testing, Industr. Robot Int. J. 37 (5) (2010) 421–426.

[16] H. Leon-Rodriguez, S. Hussain, T. Sattar, A compact wall-climbing and surface adaptation robot for non-destructive testing, 2012 12th International Conference on Control, Automation and Systems, IEEE, 2012.

[17] R. Polikar, et al., Frequency invariant classification of ultrasonic weld inspection signals, IEEE Trans. Ultrason. Ferroelectr. Freq. Control 45 (3) (1998) 614–625.

[18] C.S.N. Shitole, O. Zahran, W. Al-Nuaimy, Combining fuzzy logic and neural networks in classification of weld defects using ultrasonic time-of-flight diffraction, Insight-Non-Destruct. Test. Cond. Monit. 49 (2) (2007) 79–82.

[19] S. Sambath, P. Nagaraj, N. Selvakumar, Automatic defect classification in ultrasonic NDT using artificial intelligence, J. Nondestruct. Eval. 30 (1) (2011) 20–28.

[20] F. Margrave, et al., The use of neural networks in ultrasonic flaw detection, Measurement 25 (2) (1999) 143–154.

[21] S. Yella, M. Dougherty, N. Gupta, Artificial intelligence techniques for the automatic interpretation of data from non-destructive testing, Insight-Non-Destruct. Test. Cond. Monit. 48 (1) (2006) 10–20.

[22] A. Erhard, et al., New applications using phased array techniques, Nucl. Eng. Des. 206 (2–3) (2001) 325–336.

[23] R. DeNale, C. Lebowitz, A Comparison of Ultrasonics and Radiography for Weld Inspection, Review of Progress in Quantitative Nondestructive Evaluation, Springer 1989, pp. 2003–2010.

[24] E.A. Ginzel, Misconceptions about NDT workmanship acceptance criteria for quality control, e J. Nondestr.Test. ISSN. 19 (3) (2020)https://www.ndt.net/search/docs.php3?id=15485.

[25] A. Bulavinov, et al., Ultrasonic sampling phased array testing as a replacement for x-ray testing of weld joints in ship construction, Proceedings of the 9th International Navigational Symposium on Marine Navigation and Safety of Sea Transportation, Gdynia, Poland, 2011.

[26] M. Moles, et al., Review of ultrasonic phased arrays for pressure vessel and pipeline weld inspections, J. Press. Vessel. Technol. 127 (3) (2005) 351–356.

[27] A.D. Watkins, D.C. Kunerth, T.R. McJunkin, Eddy Current Examination of Spent Nuclear Fuel Canister Closure Welds, Idaho National Laboratory (INL), 2006.

[28] B.W. Drinkwater, P.D. Wilcox, Ultrasonic arrays for non-destructive evaluation: a review, NDT Int. 39 (7) (2006) 525–541.

[29] C. Holmes, B. Drinkwater, P. Wilcox, The post-processing of ultrasonic array data using the total focusing method, Insight-Non-Destruct. Test. Cond. Monit. 46 (11) (2004) 677–680.

[30] P. Dubois, et al., Simulation of Ultrasonic, Eddy Current and Radiographic Techniques within the CIVA Software Platform, 10th European Conference on Non–Destructive Testing, Moscow, 2010.

[31] F. Foucher, P. Dubois, Applications and recent evolutions of the CIVA Simulation Platform, 18th World Conference on Nondestructive Testing, Durban, South Africa, 2012.

[32] Y. Javadi, et al., Investigating the effect of residual stress on hydrogen cracking in multi-pass robotic welding through process compatible non-destructive testing, J. Manuf. Process. (2020) https://www.sciencedirect.com/science/article/pii/S1526612520301833?casa_token=sB5uac-c22AAAAAA:2cVf3EiOzc_WjYZEZ56XV6do0CGZ6x76F1l1kIJKfs-4NEzd5PIOeaHrANDHPwasjYrwxWIefw In press.

[33] C. Mineo, et al., Enabling robotic adaptive behaviour capabilities for new industry 4.0 automated quality inspection paradigms, 57th Annual British Conference on Non-Destructive Testing, 2018.

[34] C. Mineo, et al., Interfacing Toolbox for Robotic Arms with Real-Time Adaptive Behavior Capabilities, 2019.

[35] H. Lee, et al., Longitudinal and shear wave velocities in pure tungsten and tungsten fiber-reinforced tungsten composites, Phys. Scr. 2017 (T170) (2017), 014024, .